Excitations and magnetization density distribution in the dilute ferromagnetic semiconductor Yb_{14}MnSb_{11}

M. B. Stone, V. O. Garlea, B. Gillon, A. Cousson, A. D. Christianson, M. D. Lumsden, S. E. Nagler, D. Mandrus, and B. C. Sales

Phys. Rev. B **95**, 020412 — Published 23 January 2017

DOI: 10.1103/PhysRevB.95.020412

Excitations and magnetization density distribution in the dilute ferromagnetic semiconductor $Yb_{14}MnSb_{11}$

M. B. Stone,[1] V. O. Garlea,[1] B. Gillon,[2] A. Cousson,[2] A. D. Christianson,[1]
M. D. Lumsden,[1] S. E. Nagler,[1] D. Mandrus,[3] and B. C. Sales[4]

[1]*Quantum Condensed Matter Division, Oak Ridge National Laboratory, Oak Ridge, Tennessee 37831, USA*
[2]*Laboratoire Léon Brilloun, CEA-CNRS, CEA Saclay, 91191 Gif-sur-Yvette, France*
[3]*Department of Materials Science and Engineering, University of Tennessee, Knoxville, Tennessee 37996, USA*
[4]*Materials Science and Technology Division, Oak Ridge National Laboratory, Oak Ridge, Tennessee 37831, USA*

$Yb_{14}MnSb_{11}$ is a rare example of a Kondo lattice compound with ferromagnetic dominated RKKY interactions. As a ferromagnetic semiconductor with $T_c \approx 53$ K, it is also a potential compound for exploration of spintronic devices. Here we describe measurements which answer remaining questions regarding the energy scales of the exchange interactions, the valence and the magnetization density distribution in this system. We find that the system consists of RKKY exchange coupled Mn^{2+} sites with nearest and next nearest exchange interactions dominating the magnetic spectrum with no significant magnetization density localized on other atomic sites. The extended spread of a negative magnetization around each of the Mn ions supports a Kondo screening cloud scenario for $Yb_{14}MnSb_{11}$.

PACS numbers: 75.50.Dd, 75.40.Gb, 75.30.Et

Ferromagnetic semiconductors (FMSC) such as the epitaxially grown dilute FMSC $Ga_{1-x}Mn_xAs$[2]are a promising class of materials for spintronic devices[1]. By comparison, stoichiometric FMSCs, such as $Yb_{14}MnSb_{11}$, also have potential for device applications if the relevant energy scales and magnetic interactions can be understood. The $A_{14}MnPn_{11}$ series of compounds where A is an alkaline or rare earth element and Pn is a pnictogen provides a spectrum of materials with interesting properties. These ternary compounds exhibit behavior ranging from ferromagnetic (FM) (A=Ca, Sr, Ba and Pn=Sb)[4] and antiferromagnetic (A=Ba, Pn=Bi)[5], to colossal magnetoresistance materials (A=Eu and Pn=Sb)[6] in both metallic and semiconducting phases. Considered to be a dilute FMSC due to the low concentration of magnetic ions and low carrier concentration[7], $Yb_{14}MnSb_{11}$ has also been characterized as an excellent material for the basis of thermoelectric devices at and above room temperature.[8–10] This system also allows for a unique opportunity to measure FM excitations in the magnetic long-range-ordered phase of a material with a proposed Kondo lattice of 3d ions.[11,12]

Magnetic interactions in the $A_{14}MnPn_{11}$ series are generally considered to be RKKY type, however questions remain as to the distribution of negative magnetization, the relevant exchange paths and the potential for magnetic interactions via the pnictogen site. To fully exploit the high temperature thermoelectric behavior or low-temperature spintronic capabilities of $Yb_{14}MnSb_{11}$, one must answer these remaining quandaries. Through neutron diffraction and spectroscopy, we show that the Sb and Yb sites in $Yb_{14}MnSb_{11}$ have very weak magnetic moments ($< 0.1\ \mu_B$) and that only nearest and next nearest neighbor interactions between the Mn sites dominate the spin-dynamics.

Figure 1(a) illustrates the tetragonal crystal structure of $Yb_{14}MnSb_{11}$.[13] Mn sites tetrahedrally coordinated with Sb stack vertically along the c-axis with a spacing of $c/2 = 10.97$ Å (dashed bonds). Neighboring Mn sites are offset with vectors of the type $\pm 0.5\vec{a} \pm 0.25\vec{c}$ or $\pm 0.5\vec{b} \pm 0.25\vec{c}$ (9.956 Å) (solid blue bonds). Early thermodynamic and transport data led to the proposal that the system consists of Mn^{3+} local moments coupled via conduction electrons making the system a three-dimensional Kondo lattice with RKKY mediated exchange.[14] These studies also found that the Mn sites consist of 4.9 Bohr magneton (μ_B) local moments, although only 3.81 μ_B are ordering below $T_c = 53(1)$ K in agreement with the valence arrangement predicted value of 4 μ_B/Mn considering there is likely a small bandlinke component to the ferromagnetism. From XMCD characterization of $Yb_{14}MnSb_{11}$, it was proposed that there are antialigned Sb moments in the Sb tetrahedron surrounding Mn^{2+} sites which are causing the reduced ordered moment.[15] We find the magnetic structure and dynamics of $Yb_{14}MnSb_{11}$ are indeed well described by a Mn^{2+} valence, but there is no single site in the lattice that carries a moment antiparallel to the Mn moment. Rather a negative magnetization density is distributed among the other atomic sites.

Single crystal samples were produced with Sn flux.[7,14] Initial single crystal neutron diffraction measurements were performed using the HB1 triple-axis-spectrometer at the High Flux Isotope Reactor (HFIR) at Oak Ridge National Laboratory (ORNL). Figure 1(c) is an order parameter measurement of the (220) Bragg peak as a function of temperature.[17] Upon entering the FM phase the scattering intensity rapidly increases. We fit the data to a power law $I(T) = A + B(T_c - T)^{2\beta}$, where A is the intensity of the (220) nuclear peak and B is the amplitude of the magnetic scattering with critical exponent

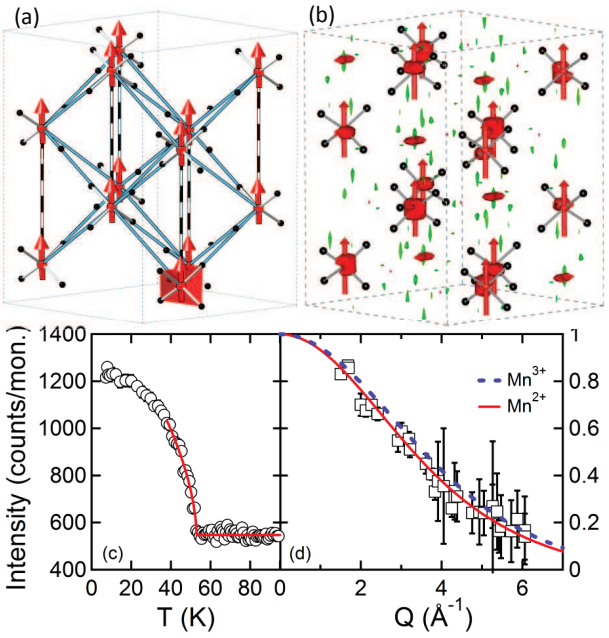

FIG. 1: (color online) (a) Crystal and magnetic structure of $Yb_{14}MnSb_{11}$ with c-axis vertical.[16] The red/black sites are the Mn/Sb sites. Only Mn and Sb(2) sites are shown for clarity.[13] The single red tetrahedron illustrates the Mn-Sb(2) coordination. The dashed grey line is the unit cell. The blue and dashed bonds between Mn sites represent J_0 and J_1 exchange. (b) Refined magnetization density superimposed on the nuclear crystal structure. Red volumes show magnetization density centered on the Mn site at a 0.025 level. Green volumes show negative magnetization density distributed within the unit cell at a 0.025 level on Yb and Sb atomic positions. (c) Intensity as a function of temperature for the (220) Bragg peak. Red line is a power law fit using $T > 35$ K data. Data were collected for approximately two seconds per point. (d) $T = 5$ K magnetic form factor as a function of wave-vector transfer for the examined magnetic reflections where only Mn sites contribute to the scattering intensity. Lines are fits using the Mn^{2+}/Mn^{3+} (red solid/dashed blue) valence. For presentation, data are binned in units of 0.25 Å^{-1} for $Q \geq 3.75$ Å^{-1}

β. The power law represents the data well as shown in Fig. 1(c) and we extrapolate a value of $\beta = 0.33(3)$ at $T_c = 52.9(1)$.[17] This value agrees with other experimental determinations in 3D Heisenberg systems.[18]

Single crystal unpolarized and polarized neutron diffraction (PND) measurements employed the 5C2 and 5C1 diffractometers at the Laboratoire Léon Brillouin with wavelengths $\lambda = 0.83$ and 0.84 Å respectively and an approximately 3x3x3 mm^3 crystal of $Yb_{14}MnSb_{11}$. A structural refinement was performed at $T = 80$ K$> T_N$ and $T = 2$ K resulting in only a 0.041(7) % contraction in the cell volume upon cooling with $T = 2$ K lattice constants $a = 16.6739(2)$ and $c = 21.9796(3)$ Å with the $I4_1/acd$ space group in agreement with literature values.[11,13] Considering only The Mn moments contributing to the magnetic reflections in the unpolarized measurement, the magnetic structure was refined to have all moments pointing along the c-axis with an ordered moment of 4(1) μ_B.[17]

The PND measurements were conducted for two sample orientations with an applied vertical magnetic field of 6 T along the c and a-axis. A Heusler monochromator provided a polarized beam of $P = 0.88$ with the polarization direction of the incident neutrons defined by a magnetic guide field. The guide field was inverted using a cryogenic flipping device. Scattering intensities I^+ and I^- were measured for incident neutrons polarized parallel (+) and antiparallel (−) with respect to the applied magnetic field. The flipping ratio $R = I^+/I^-$ was collected at $T = 2$ K for each accessible Bragg reflection to determine the magnetic structure factors. The maximum entropy method (MEM) was used to perform a model-free analysis of the magnetic structure factors for 128 reflections.[?] The MEM calculation places the overwhelming majority of the magnetization density on the Mn positions as illustrated in Fig. 1(b). There is some small negative spin density spread throughout the lattice at other atomic sites. Significantly, there is little spin density at the Sb(2) atomic site in disagreement with the proposal that this site hosts a substantial moment antiparallel to the Mn site.

A magnetic form factor was evaluated using only the reflections where the Mn site contributes. After accounting for a Debye Waller contribution, these results are shown in Fig. 1(d). There is significant statistical improvement describing the results using a Mn^{2+} form factor (reduced $\chi^2 = 1.51$) compared to the Mn^{3+} form factor (reduced $\chi^2 = 3.32$).[17,20] The magnetization density was quantitatively determined using a refinement with FULLPROF software[21]. In the refinements, the atomic position, thermal parameters and extinctions were fixed to the values obtained from the un-polarized experiment. Since the Mn moment is much larger than the potential moment on any other atomic site, a first refinement was done using only the reflections where the Mn atoms do not contribute (the condition for contribution from the Mn 8a site is $2h+l = 4n$). The magnetizations of Yb and Sb were described using a multipolar approach, but assuming a spherical distribution.[17] The obtained Yb and Sb magnetizations were then fixed in the final refinement where all the measured reflections were used (93 reflections measured with the 6 T vertical field oriented parallel to the c-axis). Only the Mn moment was refined in the final step using a Mn^{2+} (reduced $\chi^2 = 10.86$) or a Mn^{3+} (reduced $\chi^2 = 16.2$) form factor. The magnetization values for the Mn^{2+} refinement are listed in Table I. The total magnetization (sum of the magnetization at each individual site times the site multiplicity) is 3.70(7) μ_B per formula unit, consistent with the saturation magnetization 3.81(1) μ_B.[14] The magnetization density is dominated by the Mn site. The Yb and Sb sites both carry a net negative magnetization density with the Yb sites having nearly twice the contribution compared to the Sb sites. The refinement is consistent with the MEM re-

TABLE I: Values for the refinement described in the text. *The Sb(4) site was not refined because it can not be distinguished from the Mn site in its contribution to the Bragg reflections.

Atomic site	Wyckoff Pos.	M (μ_B)
Sb(1)	16f	0.020(5)
Sb(2)	32g	-0.03(1)
Sb(3)	32g	-0.004(6)
Sb(4)	8b	0*
Yb(1)	32g	-0.044(4)
Yb(2)	32g	-0.025(6)
Yb(3)	16e	-0.059(5)
Yb(4)	32g	-0.002(8)
Mn	8a	4.15(2)

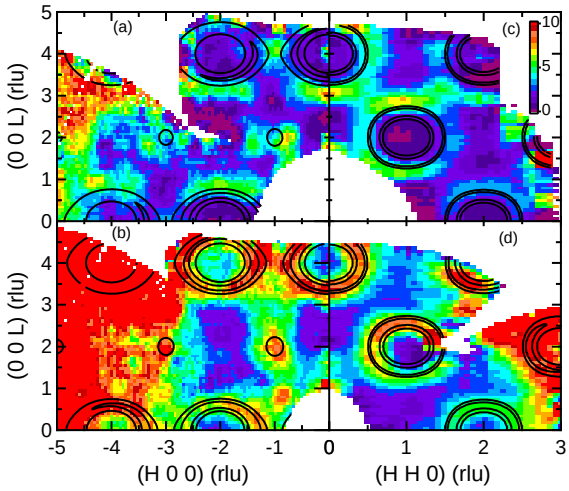

FIG. 2: (color online) $T = 5$ K single crystal INS measurements and model of the spin-wave spectra. (a) and (c) were integrated between 5 and 7 meV. (b) and (d) were integrated between 3 and 5 meV. Model spectra (see text) are overlayed as contour lines at the 75% and 25% intensity level. Data are folded about principal axes to improve statistics. Integration normal to the planes shown is +/- 0.2 rlu.

sults in that the negative magnetization is spread over all the non-Mn atoms in the lattice and not localized to the Sb(2) site coordinated to the Mn atom.

Optical, magnetic, thermodynamic, and doping studies suggest[11,12,22] that $Yb_{14}MnSb_{11}$ is an example of a ferromagnetic Kondo lattice in the underscreened limit.[23,24] The partial screening of the Mn moments by the conduction electrons occurs over a characteristic distance corresponding to the size of the Kondo screening cloud, $\xi_K = \frac{hv_f}{2\pi k_B T_K}$, where v_f is the Fermi velocity and T_K is the Kondo temperature.[25] For most bulk systems, the size of the cloud is estimated in the range between 0.1 to 1 microns, which is too large and diffuse to be easily observed. For $Yb_{14}MnSb_{11}$ the situation is more favorable since this compound is a low carrier density metal (low v_f) with a relatively high $T_K \approx 300$ K[11,12], which should result in a smaller value of ξ_K. Using the measured carrier concentration[11,12] of $1.4X10^{21}$ holes-cm^{-3} and an effective mass between the band mass of 1.8 m_0 and the low temperature Kondo enhanced mass of 18 m_0, results in $\xi_K \approx 0.5 - 5$ nm. The smaller value is about half of the nearest neighbor distance between the Mn atoms. Even using this smaller value implies that the moment compensation (Kondo cloud) is extended over all of the neighboring Sb and Yb atoms. This is consistent with the experimental observation of a small negative magnetic moment on almost all of the neighboring atoms (which adds up to -0.65(5) μ_B) as opposed to a single large negative moment on the nearest neighbor Sb atoms.

To understand the exchange interactions in the presence of this distributed negative magnetic moment, we pursued single crystal INS measurements using the ARCS spectrometer at the SNS. Measurements used two co-aligned crystals in the (H0L) scattering plane with a total mass of 1.26 grams.[17] Figure 2 shows constant energy slices from the $E_i = 15$ meV data integrated for $5 \leq \hbar\omega \leq 7$ meV in (a) and (c) and $5 \leq \hbar\omega \leq 7$ meV in (b) and (d), where $\hbar\omega$ is energy transfer. The left/right column of data are from the (H0L)/(HHL) reciprocal lattice plane. FM rings of scattering emerge from magnetic Bragg peaks. The diameter increases with increasing energy transfer. The magnetic signal is clearest at short wave-vectors with phonon scattering increasing in intensity at larger wave-vector transfer. Phonon scattering can be seen especially in the lower energy transfer data. This scattering has less clear structure due to the large number of atoms within the unit cell contributing to the phonon spectrum. The periodicity of the magnetic dispersion along the L direction is four reciprocal lattice units (rlu), while the periodicity along the $H[HH0]$ direction is two[one] rlu. This is consistent with the periodicity implied by the conditions for the Mn site occupancy. There is no indication of multiple spin-wave branches in the data.

Figure 3 shows the magnetic dispersion along three reciprocal space directions. The spectrum has a single mode extending to approximately 9.4 meV. Higher energy magnetic excitations were not observed up to 50 meV. There is a clear quadratic dispersion emerging from the FM wave-vectors. Individual constant wave-vector cuts were made throughout the volume of data. These were each fit to a single inelastic Gaussian peak. The black circular data points in Fig. 3 correspond to the peak position for the shown and equivalent wave-vectors examined. Higher resolution $E_i = 15$ meV measurements were used to look for any signs of an anisotropy gap in the spectrum. Constant energy cuts were made along the (00L), (H00), and (HH0) directions near the (004) reflection. These were individually fit with a Gaussian function to extract the mode energy, and are plotted as grey squares in Fig. 3(b) and (c). The gap in the spectrum is less than 0.5 meV in magnitude. The predicted

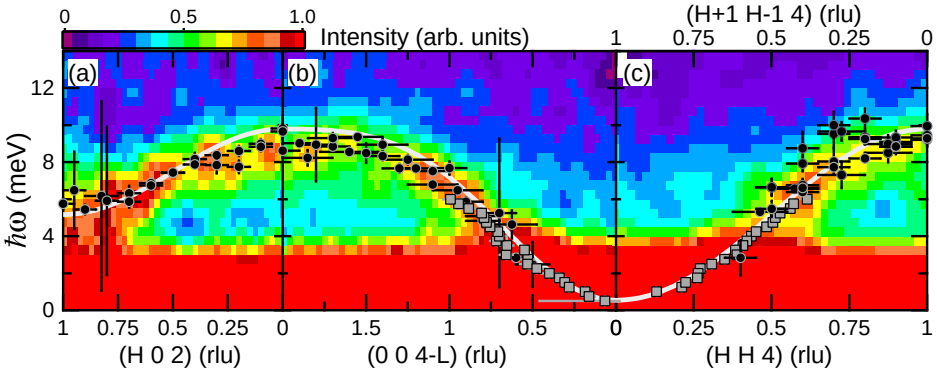

FIG. 3: (color online)$T = 5$ K single crystal $E_i = 27.5$ meV INS measurements. Data are folded about the principal axes and the $L = 4$, $L = 2$, $H = K = 0$ and $H = K = 1$ axes to improve statistics. The range of integration normal to the orthogonal axes shown is ± 0.15 for the H and K directions and ± 0.2 for the L direction. (c) Average of scattering intensity along both the (HH0) and (H+1 H-1 0) directions. Black circles are peak positions determined from fitting constant wave-vector scans. The vertical error bar is the fitted standard deviation in the peak position. The horizontal error bar is the range of integration to generate the constant wave-vector scan. Grey square points are the fitted peak positions from constant energy scans through the $E_i = 15$ meV measurement in the vicinity of the (004) magnetic Bragg peak. The horizontal error bar is the standard deviation in peak position, and the vertical error bar is the range of energy transfer used to generate the constant energy scan. The solid white line is the fitted spin-wave dispersion described in the text.

anisotropy gap based upon heat capacity measurements is slightly larger $\Delta \approx 1.1$ meV[14], although this value was determined after data correction with a significant high temperature phonon contribution.

We model the magnetic fluctuations using linear spin wave theory (LSW). Although the measurements are well in the ordered phase and the value of magnetic moment is large, deviations from the LSW model may indicate the influence of itinerancy on the spectrum. Nearest neighbor exchange interactions, J_{nn}, and next nearest neighbor interactions, J_z, are shown as solid blue and dashed bonds respectively in Fig. 1(a). Considering a FM Heisenberg Hamiltonian, one obtains the dispersion in the absence of an applied magnetic field as

$$\hbar\omega(\mathbf{Q}) = D(2S+1) + \sum_{\alpha} 2z_\alpha J_\alpha S(1-\eta_\alpha(\mathbf{Q})), \quad (1)$$

where D is energy scale of any ionic anisotropy and S is the magnitude of the spin quantum[26]. The sum in Eq. 1 is over the different exchange interactions, J_α, where z is the number of nearest neighbors of that type exchange with

$$\eta_\alpha(\mathbf{Q}) = \frac{1}{z}\sum_{\mathbf{d}_j} \exp(i\mathbf{Q}\cdot\mathbf{d}_j) \quad (2)$$

a Fourier sum over the bond-vectors $\mathbf{d}_j$, where $\mathbf{Q}$ is wave-vector transfer. For J_{nn} and J_z in $Yb_{14}MnSb_{11}$, this results in the dispersion

$$\begin{aligned}\hbar\omega(\mathbf{Q}) &= D(2S+1) + 4J_zS[1-\cos(\pi\mathrm{L})] + \\ &\quad 16J_{nn}S[1-\frac{1}{2}\cos(\frac{\pi\mathrm{L}}{2})][\cos(\pi\mathrm{K})+\cos(\pi\mathrm{H})]. \end{aligned} \quad (3)$$

Comparing Eq. 3 to the peak positions determined from more than 500 constant wave-vector and energy scans through our measurement yields $SJ_{nn} = 0.289(4)$, $SJ_z = 0.25(1)$, and $SD = 0.17(2)$ meV. For the error in the peak position, we add in quadrature five percent of the fitted FWHM of the fitted Gaussian peak to the fitted error in the peak position. Fixing the anisotropy to be zero does increase the value of reduced χ^2, and both J_{nn} and J_z are needed to account for the extent of the dispersion. The solid white line in Fig. 3 is the determined FM spin-wave dispersion in good agreement with the measurement. We also calculate the dispersion and scattering intensity in the (H0L) and (HHL) planes[27] as shown in Fig. 2. The LSW theory calculation reproduces the measured dispersion and scattering intensity reasonably well, including regions between the spin-wave cones in the (H0L) plane. We also note that there is some damping in the magnetic excitations which is causing broadening of the dispersion as seen in Fig. 3(a). This is a likely consequence of itinerancy as well as the distribution of negative magnetization throughout the crystal structure as illustrated in the PND measurements.

We have shown that the overwhelming majority of the magnetization density in $Yb_{14}MnSb_{11}$ is localized on the Mn site with the remaining magnetization density distributed among the other atomic sites. This distribution of moment is consistent with a Kondo screening cloud description. If moment were localized on another atomic site, the spin-wave dispersion would contain additional modes due to the magnetic system consisting of a lattice with a basis, although depending upon the magnitude of the additional moment such modes would be difficult to observe. There are no modes consistent with this in the measured spectra. We also find the magnetic reflections are consistent with a Mn^{2+} valence. This is in agreement with XMCD measurements[15] and density functional and band structure calculations examining the isostructural

compounds $Ca_{14}MnBi_{11}$ and $Ba_{14}MnBi_{11}$.[28] The significant exchange interactions we determine are between Mn sites that have many Yb and Sb sites between them. This serves to further explain the strong influence of substitution at these sites on the magnetic properties of $Yb_{14}MnSb_{11}$ and isostructural compounds.[29,30] Measuring the magnetic excitation spectrum should provide valuable insight into the substitution effects observed in this and isostructural compounds.

A portion of this research at ORNL's High Flux Isotope Reactor and Spallation Neutron Source was sponsored by the Scientific User Facilities Division, Office of Basic Energy Sciences, U.S. Department of Energy. B.C.S. and D.M. were supported by the U.S. Department of Energy, Office of Science, Basic Energy Sciences, Materials Sciences and Engineering Division.

[1] A. H. Macdonald, P. Schiffer, and N. Samarth, Nat. Mat. **4**, 195 (2005).
[2] S. Lee, J.-H. Chung, X. Liu, J. K. Furdyna, and B. J. Kirby, Mat. Today. **12**, 14 (2009).
[3] K. Sato, W. Schweika, P. H. Dederichs, and H. Katayama-Yoshida, Phys. Rev. B **70**, 201202(R) (2004).
[4] A. Rehr, T. Y. Kuromoto, S. M. Kauzlarich, J. Del Castillo, and D. J. Webb, Chem. Mater. **6**, 93 (1994).
[5] T. Y. Kuromoto, S. M. Kauzlarich, and D. J. Webb, Chem. Mater. **4**, 435 (1992).
[6] J. Y. Chan, S. M. Kauzlarich, P. Klavins, R. N. Shelton, and D. J. Webb, Chem. Mater. **9**, 3132 (1997).
[7] B. C. Sales, R. Jin, and D. Mandrus, Phys. Rev. B **77**, 024409 (2008).
[8] J. A. Paik E. Brandon, T. Caillat, R. Ewell, and J-P. Fleurial, Proc. Nucl. Emerg. Tech. for Space (2011).
[9] S. M. Kauzlarich, S. R. Brown and G. J. Snyder, " Dalton Trans. 2099 (2007).
[10] S. Brown, S. M. Kauzlarich, F. Gascoin, and G. J. Snyder, Chem. Mater **18** 1873 (2006).
[11] B. C. Sales, P. Khalifah, T. P. Enck, E. J. Nagler, R. E. Sykora, R. Jin, and D. Mandrus, Phys. Rev. B **72**, 205207 (2005).
[12] K. S. Burch, A. Schafgans, N. P. Butch, T. A. Sayles, M. B. Maple, B. C. Sales, D. Mandrus, and D. N. Basov, Phys. Rev. Lett. **95**, 046401 (2005)
[13] J. Y. Chan, M. M. Olmstead, S. M. Kauzlarich, and D. J. Webb, Chem. Matter **10**, 3583 (1998).
[14] I. R. Fisher, T. A. Wiener, S. L. Bud'ko, P. C. Canfield, J. Y. Chan, and S. M. Kauzlarich, Phys. Rev. B **59**, 13829 (1999).
[15] A. P. Holm, S. M. Kauzlarich, S. A. Morton, G. Dan Waddill, W. E. Pickett, and J. G. Tobin, J. Amer. Chem. Soc. **124**, 9894 (2002).
[16] K. Momma and F. Izumi, J. Appl. Crystallogr., **44**, 1272 (2011).
[17] Additional measurement and analysis details are provided in the supplemental materials.
[18] P. M. Chaikin and T. C. Lubensky, *Principles of condensed matter physics*, (Camridge University Press, Cambridge 1997).
[19] K. Burger, Powder Diffraction **13**, 117 (1998).
[20] P.J. Brown in *International Tables of Crystallography, Vol. C: Mathematical Physical and Chemical Tables*, Chap. 4.4.5, Ed. by E.Prince, 1st online edition (2006).
[21] J. Rodriguez-Carvajal, Physica B **192**, 55 (1993).
[22] K. S. Burch, E. E. M. Chia, D. Talbayev, B. C. Sales, D. Mandrus, A. J. Taylor, and R. D. Averitt, Phys. Rev. Lett. **100**, 026409 (2008).
[23] N.B. Perkins, M. D. Núñez-Regueiro, B. Coqblin, and J. R. Iglesias, Phys. Rev. B. **76**, 125101 (2007).
[24] S. K. Malik and D. T. Adroja, Phys. Rev. B **43** 6295 (1991).
[25] I. Afflec, arXiv:0911.2209v2 (2010).
[26] L-P. Lévy, *Magnetism and Superconductivity*, (Springer-Verlag, Berlin 2000).
[27] S. Toth and B. Lake, J. Phys.: Condens. Matter **27**, 166002 (2015).
[28] D. Sánchez-Portal, R. M. Martin, S. M. Kauzlarich and W. E. Pickett, Phys. Rev. B **65**, 144414 (2002).
[29] J. H. Grebenkemper and S. M. Kauzlarich, APL Mater. **3**, 041503 (2015).
[30] Y. Hu, C-W Chen, H. Cao, F. Makhmudov, J. H. Grebenkemper, M. N. Abdusalyamova, E. Morosan, and S. M. Kauzlarich, J. Amer. Chem. Soc. **138**, 12422 (2016).